

Supercapacitors using Binderless Activated Carbon Monoliths Electrodes consisting of a Graphite Additive and Pre-carbonized Biomass Fibers

N.S.M. Nor¹, M. Deraman^{1,*}, M. Suleman¹, M.R.M. Jasni¹, J.G. Manjunatha²,
M.A.R. Othman¹, S.A. Shamsudin¹

¹ School of Applied Physics, Faculty of Science and Technology, Universiti Kebangsaan Malaysia, 43600 Bangi, Selangor, Malaysia

² Department of Chemistry, FMKMCC, Madikeri, Constituent College of Mangalore University, Karnataka, India

*E-mail: madra@ukm.edu.my, mderaman113@gmail.com

Received: 30 November 2016 / Accepted: 18 January 2017 / Published: 12 February 2017

Varying amounts of graphite powder (0 to 20 wt%) are mixed as an additive with self-adhesive carbon grains, which are produced from pre-carbonized powder derived from the fibers of oil palm empty fruit bunches, a by-product from palm oil mills. The mixtures are treated with KOH and converted into green monoliths (GMs). The GMs are carbonized and activated via a multistep heating profile to produce activated carbon monolith (ACM) electrodes. X-ray diffraction, field emission scanning electron microscopy and nitrogen adsorption-desorption isotherm analysis demonstrate that the addition of graphite influences the structure, microstructure and porosity of the ACM electrode materials. Electrochemical impedance spectroscopy, cyclic voltammetry and galvanostatic charge-discharge studies show that the best frequency response of the electrodes is obtained using 4 wt% of graphite. A tremendous decrease in the equivalent series resistance (~70%) and response time (~87%) leads to an improvement of specific power by 39 % and an 8-fold increase in the maximum operating frequency (from ~0.13 Hz to ~1 Hz). Furthermore, the cells incorporating the electrodes with 4 wt% of graphite retain 50% of their capacitance up to 1 Hz. These findings show that the cheap graphite powder can be a useful additive for preparing supercapacitor electrodes from activated carbon.

Keywords: Oil palm empty fruit bunches, self-adhesive carbon grains, graphite, activated carbon monoliths, supercapacitor electrode material, electrochemical characteristics

1. INTRODUCTION

Among the variety of energy storage/conversion systems such as rechargeable batteries, fuel cells, solar cells, etc., the electrochemical capacitors or supercapacitors have attracted significant

attention for energy storage applications due to their higher specific power, longer life cycles, and lower energy losses compared to batteries [1]. These advantages have made supercapacitors a very popular energy storage device for use in many applications, especially in electronic devices and electric vehicles [2,3]. The energy storage mechanism in supercapacitors is generally governed by (i) the electrostatic accumulation of charges at the high-surface-area carbon electrode-electrolyte interface (non-faradaic), and the corresponding supercapacitor is referred as an electrical-double layer capacitor (EDLC) [4], (ii) fast and reversible redox reactions (faradaic processes) that occur between the electrolyte and the electroactive materials (pseudocapacitors or redox capacitors) [4] and (iii) a combination of both non-faradaic and faradaic mechanisms (hybrid supercapacitors) [5].

EDLCs employ a variety of carbon-based materials, such as carbon powders, carbon fibers, carbon monoliths, carbon aerogels, template carbons, carbide-derived carbons, carbon nanotubes and graphene, as electrodes [6]. Activated carbons, due to their high specific surface area (SSA) $\sim(1000-3000) \text{ m}^2 \text{ g}^{-1}$ have been most widely used as active electrode materials in EDLCs [7]. In the research and development of carbon-based materials, various biomasses, such as oil palm empty fruit bunches (EFB) [8–12], rubber wood sawdust [13] and coconut shell [14,15], have been explored as potential precursors for producing activated carbon electrodes due to their large-scale availability, ease of processing and relatively low cost. The EFB fibers can be pre-carbonized to produce self-adhesive carbon grains (SACGs) that can be converted into green monoliths (GMs) without the addition of any binding agent [16–19]. These GMs are converted into activated carbon pellets for applications as electrodes in supercapacitors [20,21]. The properties of the resulting activated carbons can be tailored by varying the type of additive materials [22–25], the electrode surface [13,21,26,27] and the synthesis procedure [10,11,23,24,28,29].

Recently, a trend has emerged in research and development on carbon-based electrodes for supercapacitors, wherein graphite, carbon black, graphene and/or carbon nanotubes (CNTs) are used as additives in pristine carbons or activated carbons (chemically/physically treated carbons) to improve the electrical conductivity and porosity of the electrodes for the betterment of the supercapacitor performance. Due to their high electrical conductivity and predominant mesoporous character, these carbon additives play a significant role in enhancing the power and cycle life of supercapacitors [30,31]. Generally, the addition of graphite and carbon black [32], graphene [33], and/or CNTs [34] to activated carbons requires a binder, which leads to reduced porosity due to the masking/blocking of some pores. However, some studies have reported on composite electrodes of activated carbon and graphite [35], graphene [29,36,37] or CNTs [38–40] prepared without a binder. The relatively high cost and complex synthesis of graphene and CNTs limit their large-scale production [41–43]. Moreover, graphene or CNTs may undergo aggregation and agglomeration during mixing with activated carbon, thereby degrading the performance of the resulting composite electrodes [44]. Graphite powder is a cost-effective and readily available material and may be a better substitute to replace graphene or CNTs, thus alleviating the associated issues.

In this paper, we present a new approach for preparing binder-free ACMs electrodes from SACGs loaded with various amounts of graphite powder prior to carbonization and activation of GMs. The GMs were prepared from SACGs derived from the pre-carbonized EFB incorporated with varying quantity of graphite additives. The effect of adding graphite to the GMs is reflected in the physical and

electrochemical properties of the ACMs, and the performance of the supercapacitor cells constructed with these modified ACMs electrodes was improved, particularly in terms of the power delivery capability/frequency response.

The ACMs electrodes were characterized using various techniques, including field emission electron microscopy (FESEM), N₂ adsorption-desorption, and X-ray diffraction (XRD), and the electrochemical performance of the corresponding EDLC cells was tested using electrochemical impedance spectroscopy (EIS), cyclic voltammetry (CV) and galvanostatic charge-discharge (GCD). Regarding the novelty of this approach, the use of graphite as a carbon additive to host-precursor namely pre-carbonized EFB fibers before carbonization and activation to produce supercapacitor electrodes has not yet been reported.

2. EXPERIMENTAL

2.1 Preparation of binderless activated carbon electrodes

ACMs were prepared from EFB fibers according to our method reported previously [17]. Briefly, the fibers were pre-carbonized at a temperature of ~280 °C, followed by ball milling for approximately 18 h and then sieving to produce a powder of SACGs with a particle size less than 106 μm [8,28]. Table 1 presents the various compositions prepared from the mixture of SACGs, KOH and graphite (Hamburg Chemical GmbH) (represented as S0, S4, S8, S12 and S20).

Table 1. Various compositions of the SACGs, KOH and graphite mixtures.

Samples	Weight Percentage			
	SACG: g (wt%)	KOH: g (wt%)	Graphite: g (wt%)	Mixture: g
S0	14.25(95)	0.75(5)	0.0 (0)	15
S4	13.65(91)	0.75(5)	0.6 (4)	15
S8	13.05(87)	0.75(5)	1.2 (8)	15
S12	12.45(83)	0.75(5)	1.8 (12)	15
S20	11.25(75)	0.75(5)	3.0 (20)	15

Each composition (15 g) was separately poured into 150 ml distilled water, stirred for 1 h and then dried in an oven at 100 °C for 48 h. To ensure homogeneous mixing, each composition was milled for 20 min. To prepare GMs corresponding to each composition, 0.75 g of the mixture was loaded inside a mold (20 mm in diameter) and then pelletized using 8 metric tons of compression force. The respective GMs were carbonized at ~800 °C under a N₂-atmosphere (at a flow rate of 1.5 l min⁻¹) to produce the carbon monoliths [26,27]. A multi-step activation technique, implemented in our previous work to produce crack-free monolithic samples [45], was also used here. The carbon monoliths were activated by CO₂ at ~800 °C (at a flow rate of 1 l min⁻¹) by raising the temperature from room temperature to ~800 °C at a rate of 5 °C min⁻¹. Thus, the respective ACMs corresponding to each composition (S0, S4, S8, S12 and S20) were produced and labeled as ACM0, ACM4, ACM8, ACM12 and ACM20 (Table 2).

Table 2. Weights and dimensions of the ACMs (average values from 4 samples).

ACMs	Weight (g)	Thickness (mm)	Diameter (mm)	Density (g cm ⁻³)
ACM0	0.298	1.72	14.68	1.02
ACM4	0.319	1.62	14.94	1.10
ACM8	0.338	1.65	15.19	1.13
ACM12	0.367	1.67	15.58	1.15
ACM20	0.381	1.65	15.82	1.16

2.2 Physical characterization

XRD patterns of the graphite and various ACMs samples were recorded using a Bruker AXS D8 advance diffractometer that employed CuK α radiation (wavelength (λ) of 1.5406 Å) for an angular diffraction range (2θ) of 0° to 70°. The carbon micro-crystallite dimensions (stack height = L_c and stack width = L_a) can be calculated from the XRD diffraction pattern using the Debye-Scherrer equation, $L_c = 0.90\lambda/\beta\cos(\theta_{002})$ and $L_a = 1.94\lambda/\beta\cos(\theta_{100})$, where β is equal to the peak width at half maximum [22]. The interlayer spacings d_{002} and d_{100} of the carbon micro-crystallites can be determined from the XRD spectra using the Bragg equation, $n\lambda = 2d\sin\theta$, where $n = 1$, $\lambda = 1.5406$ Å of the X-ray radiation, and θ is the Bragg angle representing the position of the (002) and (100) diffraction peaks [22].

The N₂ adsorption-desorption isotherm data of the ACMs were recorded at -196 °C using an accelerated surface area and porosimeter system (ASAP 2010, Micromeritics). The porosity parameters, including the Brunauer-Emmett-Teller (BET) specific surface area (S_{BET}), the micropore surface area (S_{micro}), the mesopore surface area (S_{meso}), the micropore volume (V_{micro}), the mesopore volume (V_{meso}) and the average pore diameter (D_p), were determined from these isotherm data according to the BET and Dubinin-Radushkevich equations by assuming the cross-sectional area of a nitrogen molecule to be 0.162 nm² [46].

The microstructures of the ACMs were investigated by recording the micrographs of the fracture surface of the ACMs using a FESEM instrument (Supra PV 55 model) at an accelerating voltage of 3 kV. FESEM micrographs were recorded for both low (2.5×10^3 X) and high (50×10^3 X) magnifications.

2.3 Fabrication of supercapacitor cells

The ACM electrodes were prepared by polishing the ACMs to the desired thicknesses (~0.4 mm) and then extensively washed with distilled water until pH 7 was reached. The diameter, thickness and weight of the ACMs were 15 mm, 0.4 mm and 40-60 mg, respectively. Each fabricated cell consisted of two ACMs electrodes, an electrolyte (1 M aqueous H₂SO₄), a polypropylene separator (Celgard 3501, ~25 μm thickness) fully wetted with electrolyte and two stainless steel current collectors (316-L stainless steel foils of ~0.05 mm thickness, Goodfellow Cambridge Ltd., England). These components were stacked between two pieces of Perspex casing and compactly assembled due to the inward forces of a clamp.

2.4 Electrochemical characterization

The performance of the supercapacitor cells was tested using three techniques, namely EIS, CV and GCD, using a Solartron 1286 electrochemical interface. All measurements were performed at room temperature. From the EIS data, the specific capacitance, C_{sp} , of the electrodes was determined using the equation [11]:

$$C_{sp} = -\frac{1}{2\pi f Z'' m} \quad (1)$$

where f is the lowest frequency, and Z'' is the imaginary impedance at f . The EIS data as a function of frequency were analyzed using the following equations:

$$Z(\omega) = Z'(\omega) - jZ''(\omega) \quad (2)$$

$$Z''(\omega) = \frac{-Z'(\omega)}{\omega |Z(\omega)|^2} \quad (3)$$

$$Z'(\omega) = \frac{Z''(\omega)}{\omega |Z(\omega)|^2} \quad (4)$$

where $Z(\omega) = 1/j\omega C(\omega)$, C' is the real capacitance, C'' is the imaginary capacitance, Z' is the real impedance, and Z'' is the imaginary impedance.

From the CV data, the C_{sp} of the cells was determined using the equation [11]:

$$C_{sp} = \frac{2i}{ms} \quad (5)$$

where i is the electric current, s is the scan rate, and m is the mass of the electrode.

From the GCD data recorded at a current density of 10 mA cm⁻², the C_{sp} of the cells was determined using the equation [11]:

$$C_{sp} = \frac{2i}{\left(\frac{\Delta V}{\Delta t}\right)m} \quad (6)$$

where Δt is the discharge time and ΔV is the voltage. In addition, the values of the specific power (P) and specific energy (E) were calculated from the GCD data using the respective equations given below:

$$P = \frac{Vi}{m} \quad (7)$$

$$E = \frac{Vit}{m} \quad (8)$$

where i is the discharge current, V is the voltage excluding the iR drop at the beginning of the discharge, and t is time.

3. RESULTS AND DISCUSSION

3.1 Physical characterization

3.1.1 FESEM

To study the changes in the surface morphology of the ACM electrode materials due to the graphite addition, FESEM images were recorded. Fig. 1 (a) to (d) show FESEM micrographs of the fractured surface of ACM0, ACM4, ACM8 and ACM12 samples recorded at low magnification ($2.5 \times 10^3 \text{ X}$). The rough surface of the grains, rough grain boundaries and smooth surfaces shown in these micrographs signify the porous characteristics of the samples made of microstructures with a network of open pores. A comparison of the micrograph of Fig. 1 (a) with those in Fig. 1 (b) to (d) indicates that no obvious changes in the ACM microstructure occur at this scale.

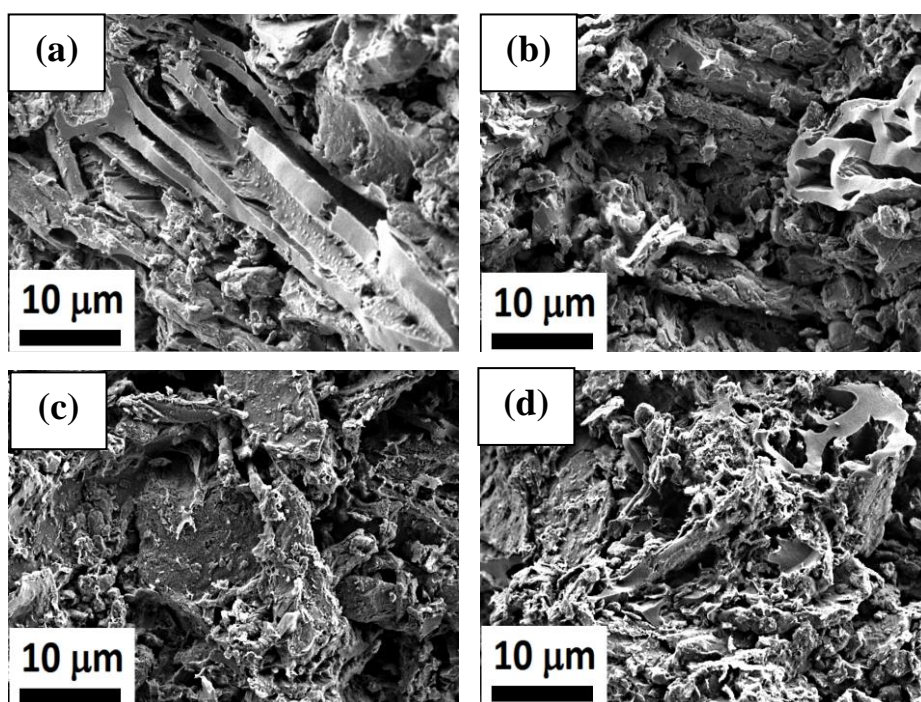


Figure 1. FESEM images of the fractured surface of (a) ACM0, (b) ACM4, (c) ACM8 and (d) ACM12 electrodes at low magnification ($2.5 \times 10^3 \text{ X}$).

FESEM micrographs of the fractured surfaces of all the samples were also recorded at higher magnification ($50 \times 10^3 \text{ X}$) as shown in Fig. 2 (a) to (d). The microstructure of the ACMs with open pore network distributed evenly all over the samples can be seen in these high magnification micrographs. The effect of graphite additive in the ACMs is still not visible at this scale as can be seen that all the micrographs are almost indistinguishable. There are no considerable differences among these four images, indicating that the effect of graphite additive on the electrodes properties occurs at the scale of microcrystallite size, which is beyond the resolution range of FESEM. It should be mentioned here that the changes in microcrystallites size can be more clearly observed and quantified using X-ray diffraction analysis. Further, the changes in microcrystallite size are also in good

agreement with the changes in surface area and other porosity parameters as evaluated from N₂ adsorption-desorption isotherm discussed in subsequent section.

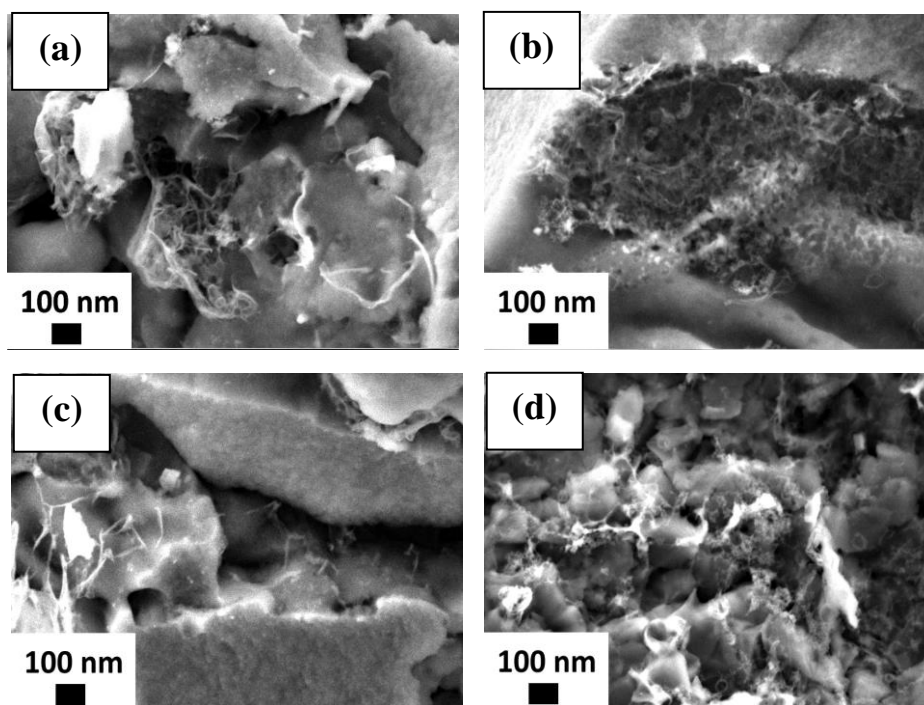


Figure 2. FESEM images of the fractured surface of (a) ACM0, (b) ACM4, (c) ACM8 and (d) ACM12 electrodes at high magnification ($50 \times 10^3 X$).

3.1.2 X-ray diffraction

Fig. 3 shows the comparative XRD patterns of the ACM0 electrode and the electrodes containing graphite additive (ACM4, ACM8 and ACM12). The broad peaks (base of the 002 graphite sharp peak) at $2\theta \approx 25^\circ$ and $2\theta \approx 43^\circ$ for the ACM0 sample are due to the 002 and 100 diffraction planes associated with the turbostratic structure of the carbon material [22]. This is a typical structure of activated carbon from biomass. For the ACMs samples containing graphite, as expected, sharp peaks at $2\theta \approx 26^\circ$ are appeared, which are due to the 002 plane of the graphite structure. The 002 graphite peaks seem to shift to higher 2θ values, indicating a decrease in the interlayer spacing of the graphite due to the carbonization and activation processes. A similar trend is shown by the 002 broad peak of the activated carbon from the SACG component in the GMs. The 002 graphite peaks become higher with broader bases as the graphite content in the ACMs increases, indicating that the crystallite dimension of the graphite changed after undergoing carbonization and activation with the SACGs.

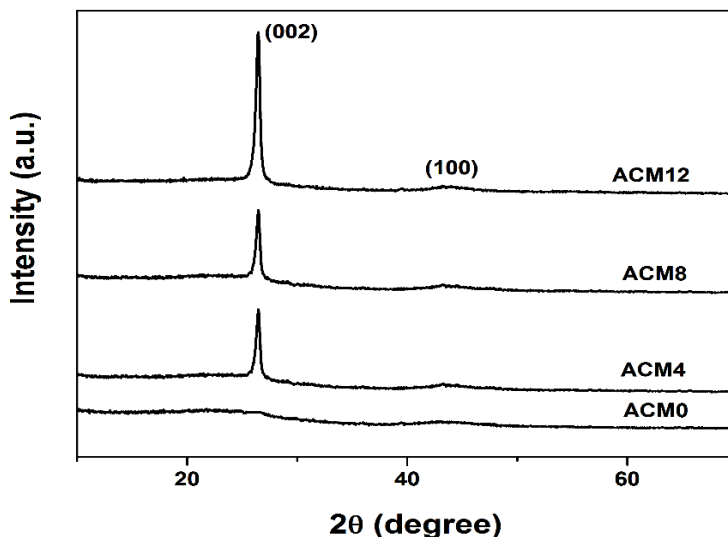


Figure 3. XRD patterns for ACM0, ACM4, ACM8 and ACM12 electrodes.

Various structural parameters determined from the XRD data in Fig. 3 (using the procedure mentioned in experimental section) such as the interlayer spacing (d_{002} and d_{100}) and the microcrystallite dimensions (L_a and L_c), of ACM0 and the ACMs with graphite additives are presented in Table 3. The decrease in the interlayer spacing, the increase in the mean number of planes, N_p (given by L_c/d_{002}), and the relative density of the edge and basal planes (L_c/L_a) in the microcrystallites indicate the restoration of more ordered carbon with predominant sp^2 graphitized domains. The results shown in Table 3 and Table 4 indicate that the S_{BET} values decrease as the crystallite size decreases due to the increase in the graphite content of the electrode. The decreases in the S_{BET} values appear to be proportional to the decrease in the crystallite sizes of the electrodes. It has been reported elsewhere that there is a strong dependency of the S_{BET} on the variation of crystallites dimension of carbon electrodes resulted from the incorporation of addition of CNTs [9,10] and petroleum coke [22] additives in the electrodes. The changes of the structures of the modified electrodes with respect to ACM0 leads to improved performance of the EDLC cells, particularly in terms of power, ESR , capacitance retention and frequency response, as discussed later.

Table 3. Interlayer spacing, crystallite dimension and ratios of L_c/L_a and L_c/d_{002} for all of the ACMs electrodes.

ACMs	d_{002} (nm)	d_{100} (nm)	L_c (nm)	L_a (nm)	L_c/L_a	L_c/d_{002}
ACM0	4.22	2.15	10.40	61.21	0.16	2.46
ACM4	3.94	2.11	11.19	52.18	0.21	2.84
ACM8	3.86	2.12	11.22	36.98	0.30	2.90
ACM12	3.70	2.05	11.32	28.68	0.39	3.05

3.1.3 N₂ adsorption-desorption isotherms

Fig. 4 shows the comparative N₂ adsorption-desorption curves for the reference sample (ACM0) and the samples containing graphite (ACM4, ACM8 and ACM12) recorded at -196 °C. All of the curves show similar patterns representing a combination of both type I and type IV isotherms, according to the IUPAC classification. These patterns demonstrate that carbon material possesses a porous network containing both micropores and mesopores, with a high internal surface area [47,48].

Quantitative estimations of various porosity parameters including S_{BET} , S_{micro} , S_{meso} , V_{micro} , V_{meso} and D_p determined from the isotherms data are presented in Table 4. A comparison shows that the addition of graphite into the GMs results in reduced values of S_{BET} , S_{micro} , S_{meso} and V_{micro} for all ACMs containing graphite. Increasing amounts of graphite in the GMs were found to show a corresponding decrease in specific surface area of all of the compositions. This decrease may be due to the fact that a relatively larger fraction of micropores are occupied by the graphite particles. However, the values of D_p and S_{meso}/S_{micro} for ACMs composited with graphite are higher than ACM0 and maximum for ACM4. This modification in the porosity properties of the electrodes is expected to affect the performance of the EDLC cells in terms of enhanced power, ESR, capacitance retention and frequency response, which would be discussed in later sections.

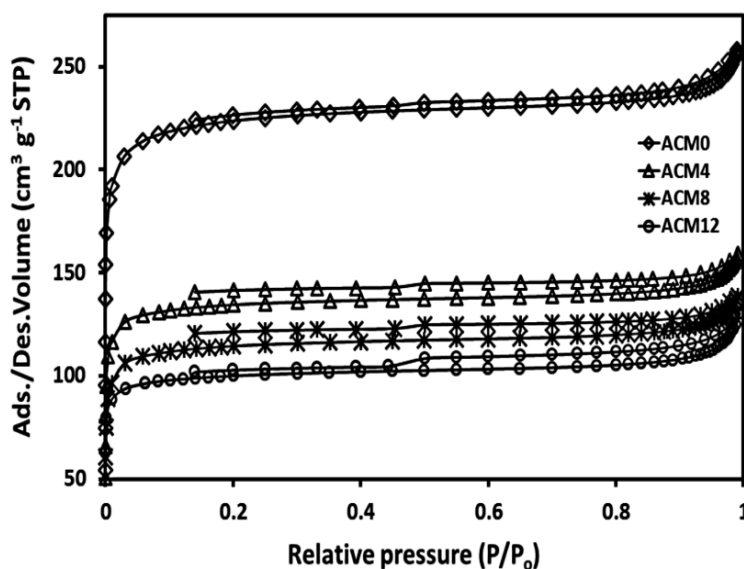


Figure 4. N₂ adsorption-desorption isotherms for ACM0, ACM4, ACM8 and ACM12 electrodes.

Table 4. Pore characteristic parameters for ACM0, ACM4, ACM8 and ACM12 electrodes.

Samples	ACM0	ACM4	ACM8	ACM12
S_{BET} (m ² g ⁻¹)	744	400	360	330
S_{meso} (m ² g ⁻¹)	110	92	70	50
S_{micro} (m ² g ⁻¹)	687	308	290	280
V_{meso} (cm ³ g ⁻¹)	0.05	0.09	0.07	0.06
V_{micro} (cm ³ g ⁻¹)	0.30	0.15	0.16	0.17
D_p (nm)	2.00	3.25	2.20	2.10
S_{meso}/S_{micro}	0.16	0.30	0.25	0.18

3.2 Electrochemical characterization

3.2.1 Specific Capacitance

Fig. 5 (a), (c) and (d) shows the data recorded from the EIS, CV and GCD tests, respectively, for Cell-0, Cell-4, Cell-8, Cell-12 and Cell-20. Fig. 5 (a) shows the Nyquist plots of all of the cells in the frequency range from 1 MHz to 10 mHz, with an enlarged view of the high frequency region in the inset. The plots consist of capacitive (nearly vertical line-line 1) signal, resistive-capacitive (Warburg line-line 2) signal and resistive (semicircle-line 3) signal in the low, intermediate and high frequency regions, respectively as shown by the schematic diagram in Fig. 5 (b). The behavior of this plot is typical for carbon-based supercapacitors. This behavior seems to be affected by the quantity of graphite additive in the electrodes.

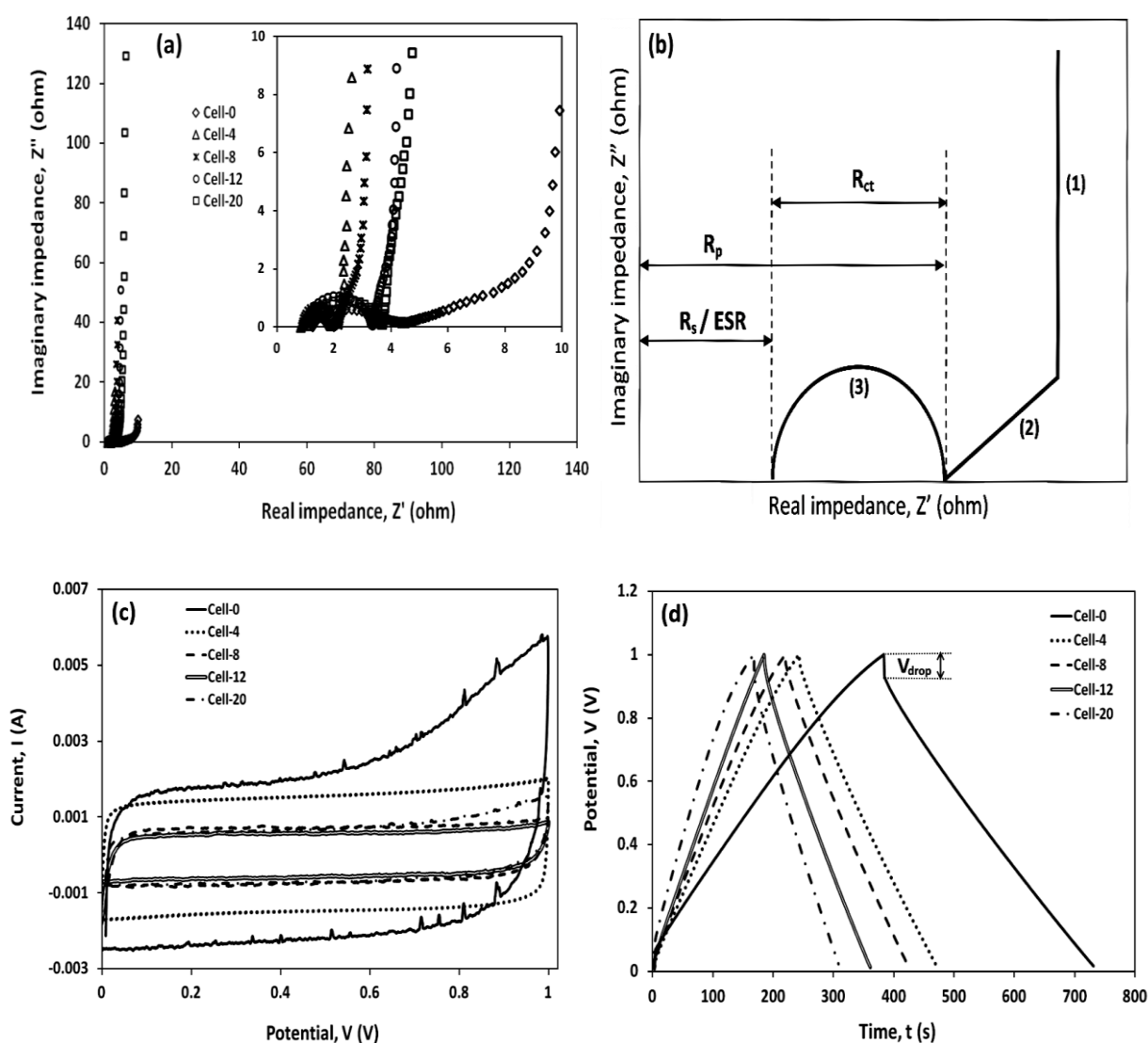


Figure 5. The electrochemical performance of the cells: (a) Nyquist plots from EIS, (b) Schematic diagram of figure (a), (c) CV curves at 1 mV s^{-1} and (d) GCD curves at 10 mA cm^{-2} .

Fig. 5 (c) shows the cyclic voltammograms recorded at room temperature at a scan rate of 1 mVs⁻¹ over a potential window ranging from 0 to 1 V. The near rectangular shape of the voltammograms of all of the cells indicates electric double-layer behavior and is similar to typical voltammograms reported in the literature [32]. More rectangular shapes of the CV curves for Cell-4, Cell-8, Cell-12 and Cell-20 demonstrate relatively less electronic resistance and better ion transport in composite electrodes. Furthermore, of all of the cells, Cell-4 exhibits the best CV profile closest to the ideal behavior. This is attributed to the fast ion switching behavior and quick double-layer formation due to the most appropriate porous structure of the ACM-4 electrodes. Fig. 5 (d) shows the charge-discharge curves recorded from the GCD test at a constant current load of 10 mA cm⁻². All of the curves show a typical triangular behavior with different duration of the charge/discharge time, depending on the quantity of the graphite additive in the electrodes.

Fig. 6 (a) shows that the specific capacitance values of all the cells based on the data extracted from EIS, CV and GCD studies and calculated using equations (1), (5) and (6) are in a good agreement. As expected, the C_{sp} value decreases because the S_{BET} of the electrodes decreases with increasing quantities of graphite in the electrodes (Fig. 6 (b)).

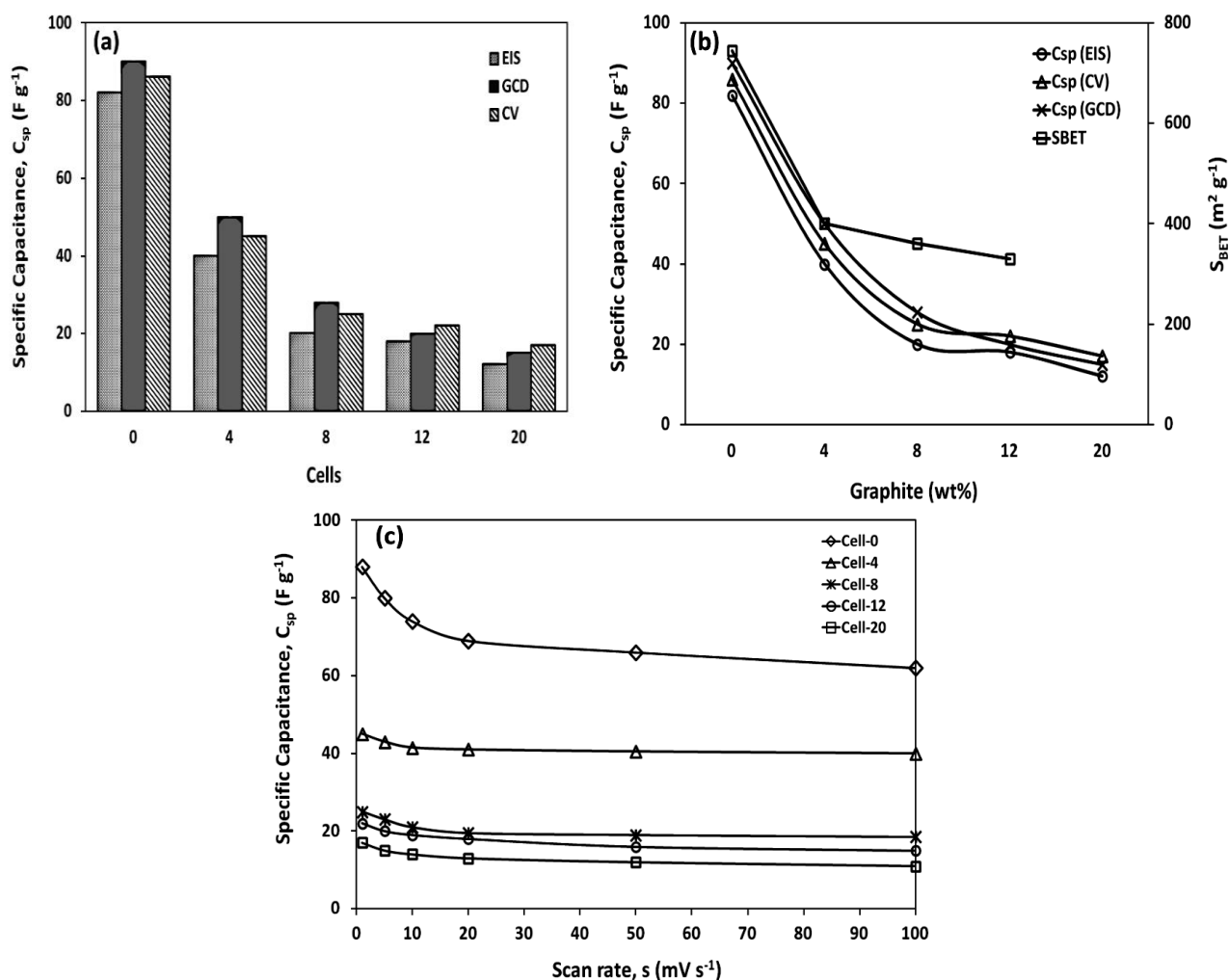


Figure 6. (a) Histogram for calculated C_{sp} from EIS, CV and GCD data (b) correlation between C_{sp} and S_{BET} versus the additive and (c) C_{sp} versus scan rate

The C_{sp} values from the CV data recorded at scan rates of 1, 5, 10, 20, 50 and 100 mV s^{-1} for all cells were calculated using equation (5), and the corresponding results are shown in Fig. 6 (c). The cell with the ACM-0 electrode exhibits ~70 % capacitance retention, and the capacitance retention is improved to the maximum value of 90 % up to the scan rate of 100 mV s^{-1} for the cell with the ACMs electrodes containing graphite additive. This level of retention is higher (65-90 %) than the retention levels of carbon composite electrodes containing CNT (26-44 %) [9], graphene (67 %) [33], graphene oxide [49], graphite (40-50 %) [30] and carbon black (75-85 %) [30] as additives, as reported previously. Generally, this decrease in capacitance at higher scan rates is very common for carbonaceous materials and higher for the electrodes containing larger proportions of the deepest micropores/bottle neck pores, which takes relatively more time for ion diffusion and adsorption [50]. Therefore, these results indicate that the larger proportion of mesopores in the electrodes containing graphite facilitates ion transportation during charging and discharging and leads to a significant improvement in preventing the decay of C_{sp} with increasing scan rates, even though the C_{sp} of the cells decreases due to the presence of graphite in the electrodes.

The values of S_{BET} , C_{sp} and charge transfer resistance, R_{ct} from the present study are compared with values reported in previous studies involving the use of other types of carbon additives, such as CNT [9,10,34,38,51,52], graphene [29,33,53,54], petroleum coke [55], graphene oxide [56] and carbon black [30] in supercapacitor-activated carbon electrodes (Table 5). It is clearly shown in this table that the use of this cheap graphite additive could produce results that are competitive compared to the results generated using other expensive additives such as CNT and graphene.

Table 5. The S_{BET} , C_{sp} and R_{ct} values of the carbon electrodes.

Electrodes	Additive (wt%)	S_{BET} ($\text{m}^2 \text{g}^{-1}$)	C_{sp} (F g^{-1})	R_{ct} (ohm)	Ref.
From carbonization of binderless GMs containing graphite	0 - 20	330 – 744	12 – 90	1.02 – 2.40	Present study
From carbonization of binderless GMs containing CNT	0 - 6	987 – 1596	86 – 111	0.26 – 1.46	[9]
	0 and 5	369 – 1656	10 – 133	0.14 – 5.74	[10]
	0 and 5	415 – 485	55 – 85	0.20 – 0.32	[38]
From carbonization of binderless GMs containing petroleum coke	0 - 70	53 – 448	1.9 – 23	0.30 – 1.65	[55]
From carbonization of binderless GMs containing graphene	0 - 10	419 – 798	*50 – 113	-	[29]
Composite of activated carbon and CNT using binder	0 - 6	865 – 1120	105 – 145	0.31 – 0.37	[51]
	0 – 7	1000	-	1.3 – 6.9	[52]
	0 and 10	250 – 1626	120 – 200	0.01 – 0.12	[34]
Composite of activated carbon and graphene using binder	0 and 10	1600 – 2106	76 – 210	0.31 – 0.41	[33]
	0 and 2	1900	40 – 129	0.15 – 0.55	[53]
Composite of activated carbon and graphene oxide using binder	0 – 9	1315 – 2566	230 – 255	0.6 – 0.8	[56]
Composite of activated carbon and carbon black using binder	0 - 80	16 – 1856	73 – 130	4.5 – 6.5	[30]

Note: *The values determined from GCD data.

3.2.2 Resistance and response time

Fig. 5 (b) shows the schematic diagram (corresponding to Fig. 5 (a)) labeled with R_s (bulk electrolyte resistance/*ESR*), R_p (internal resistance of the electrode), R_{ct} (charge transfer resistance, $R_p - R_s$), W (Warburg line) and f_k (knee frequency). The values of *ESR* in the present study are comparable to the typical values of H_2SO_4 electrolyte bulk resistance (0.1 - 13 ohm) [57,58] and vary slightly depending on the quantity of graphite in the electrodes, which is predominantly due to the contact resistance between the current collector and the electrode. The R_{ct} values in this table also change with variations in the graphite quantity in the electrode, and the change in the R_{ct} parameters values are related in general to various factors, for instance, the current collector/active material interface contact resistance, the resistance in between the electrode particles, the relative sizes of ions and pores, pore depth, etc., [59,60]. Therefore, as shown in Table 6, the presence of varying quantities of graphite additive in the activated carbon matrix significantly influences the parameter values.

The Warburg line plotted in Fig. 5 (a) provides information about the electrical distributed resistance (*EDR*) due to ion diffusion in the porous network of electrode, which can be determined from the Z' -intercept of the extrapolated of the Warburg line. The *EDR* values obtained are shown in Table 6. Fig. 5 (a) shows that the lengths of the Warburg line exhibit optimum behavior with the variations in graphite content, and this behavior is consistent with the variation in *EDR* with respect to the change in the graphite content. Because shorter lengths of the Warburg line and smaller *EDR* values are known to correspond to lower resistive paths for ionic diffusion into pores, these EIS results indicate that the addition of graphite contributes to the creation of pores that are conducive for the diffusion of electrolyte ions to occupy the pores. The efficiency of ionic mobility to diffuse into micropores is known to be strongly influenced by the mesopores which act as transport pores allowing ions to reach micropores with less resistance [61]. This influence is seen in our results expressed in terms of the plots (Fig. 7) that correlates the *EDR* and R_{ct} with the ratio of S_{meso}/S_{micro} , and indicates that the lowest resistance corresponds to the electrodes having the highest mesoporous surface area or volume.

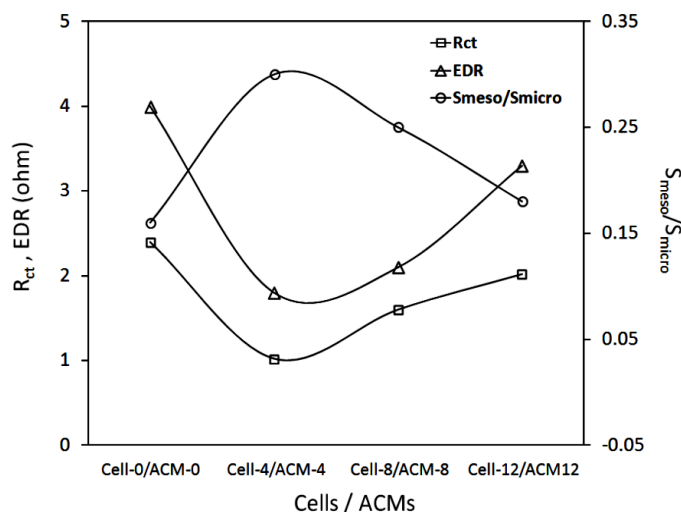


Figure 7. The plot of *EDR* and R_{ct} against the ratio of S_{meso}/S_{micro} of the electrodes.

Fig. 8 (a) shows the plot of *ESR* as a function of frequency. Here, the dotted line just above the frequency axis represents the behavior of an ideal capacitor. In general, for a supercapacitor, the *ESR* represents the effective resistance contributed by the bulk ionic resistance of the electrolyte, the ionic diffusion resistance inside micropores/bottle neck micropores, the bulk resistance of electrode material, electrode particle-particle contacts, particle-current-collector contacts, the bulk current collector and the external wires [62]. In our case, the changes in *ESR* with frequency, as shown in this figure, are associated with increases in electronic conductivity and changes in porosity due to the addition of graphite.

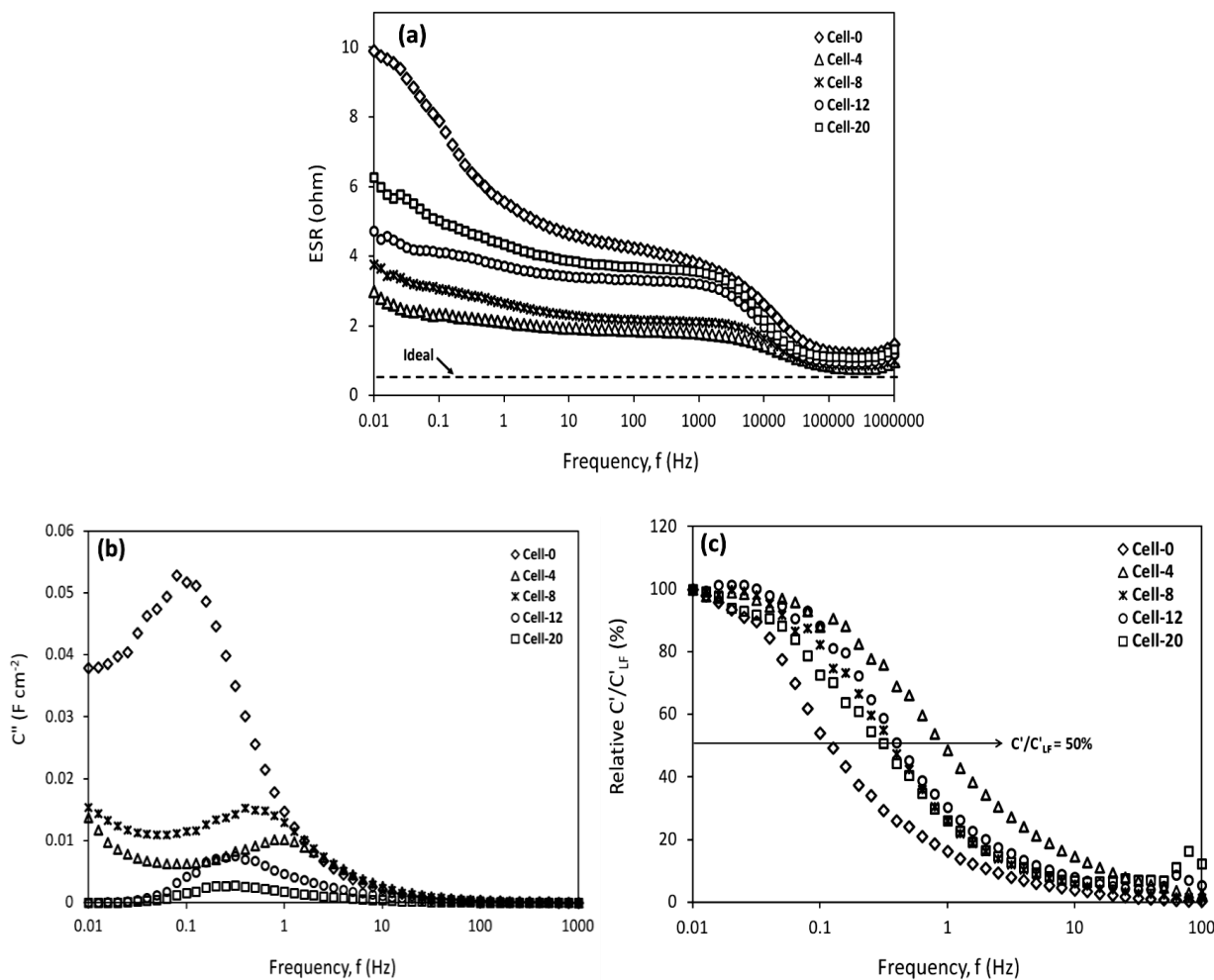


Figure 8. The characteristic frequency response of the cells: (a) *ESR* versus frequency, (b) imaginary specific capacitance versus frequency and (c) relative specific capacitance (C'/C'_{LF}) versus frequency.

The *ESR* of each cell can also be evaluated from the voltage drop of the GCD curves shown in Fig. 5 (d) and the results are shown in Table 6. These results show that the addition of graphite influences the initial voltage drop that results in decreased *ESR* values compared to the Cell-0. The minimum value of *ESR* is observed for Cell-4, which corresponds to the maximum decrease of (~70 %) with respect to Cell-0. Table 6 shows that this behavior of *ESR* values is in good agreement with the *ESR* values from the EIS. The correlation between the *ESR* (from GCD data) and the response time constant, τ_o , is

presented in Fig. 9. The minimum values of the *ESR* and τ_o for Cell-4 shown in Table 6 result in better power performance and an improved frequency response. The values of *ESR* in the present study are comparable to the recently reported values (1.2-8.8 ohm) for electrodes composed of activated carbon and graphite [35] and CNTs [40].

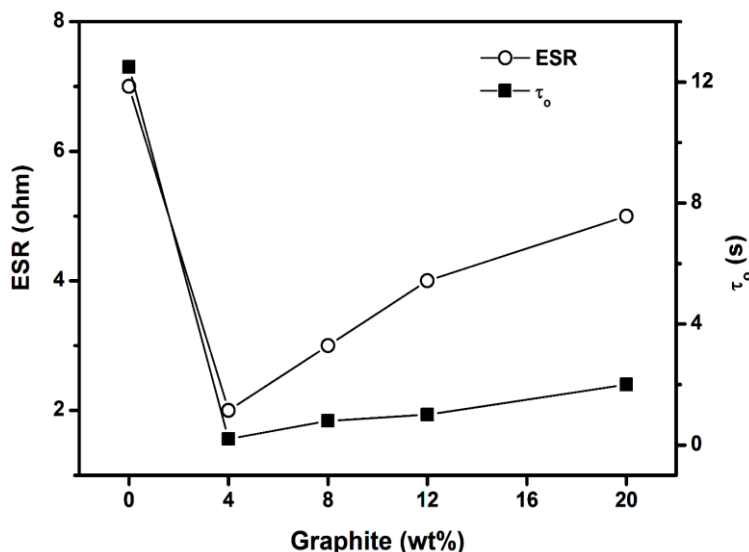


Figure 9. The correlation of the *ESR* and τ_o as functions of graphite content (wt%).

Table 6. The electrical parameters values from the Nyquist plot and the GCD data for all of the cells.

Parameters	Cell-0	Cell-4	Cell-8	Cell-12	Cell-20
R_s / <i>ESR</i> (ohm)	1.48	0.98	1.00	1.21	1.34
R_p (ohm)	1.50	0.80	0.86	1.00	1.10
R_{ct} (ohm)	2.40	1.02	1.60	2.02	2.04
<i>EDR</i> (ohm)	4.00	1.80	2.10	3.30	3.60
f_k (Hz)	0.03	0.50	0.50	0.32	0.50
<i>ESR</i> (ohm) (GCD)	~7	~2	~3	~4	~5
f_o (Hz)	0.13	1.00	0.39	0.37	0.31
τ_o (s)	7.69	1.00	2.56	2.70	3.23

The frequency responses of the cells were evaluated based on the EIS analysis in terms of the response time, τ_o ($\tau_o = 1/f_o$), from the plot of $C''(\omega)$ versus frequency, as shown in Fig. 8 (b). The τ_o values were determined from the frequency corresponding to the peak of $C''(\omega)$ in Fig. 8 (b), and the values of the characteristic τ_o are listed in Table 6. As shown in Table 6, the addition of graphite also improved the values of τ_o . Cell-4 presents the minimum value of 1 s, as opposed to the maximum value of 7.69 s for Cell-0. These τ_o values are comparable to those reported for activated carbon-based supercapacitors (1-67 s) [10,21,38,63]. In fact, τ_o is an important parameter that defines the time required to uptake/deliver power/energy [59]. Thus, Cell-4 can deliver the stored energy very quickly (in 1.00 s) as opposed to Cell-0, which will requires 7.69 s to deliver the same energy.

Fig. 8 (c) displays the plots of the real capacitance, C/C'_{LF} , as a function of frequency for all of the EDLC cells, where the C'_{LF} is the value capacitance correspond to the lowest frequency value of the respective cell. As expected, Fig. 8 (c) shows that, at substantially high frequencies, a very small capacitance is detected because the AC signal cannot penetrate deeper inside the pores and only the outer surface near the pore opening is sensed. As a result, a small area of the electrode surface is utilized. In the intermediate frequency region, a dull variation in capacitance is observed. Finally, at the lowest frequency domain when the penetration depth is higher than the pore length, the maximum number of ions reach the core of the pores utilizing most of the pore surface, and equilibrium is reached; eventually, the maximum/saturated capacitance is achieved. For Cell-0, the capacitance in the low frequency region never reaches a plateau (equilibrium), whereas the other cells show the plateau that ends at different frequency values depending on the quantity of graphite in the electrodes. This result demonstrates that the ACM-0 electrode is not fully accessible to the ions/electrical signals, even at very low frequencies. A similar trend showing inaccessibility of ions/electrical signals into the porous network of electrodes is observed elsewhere [64]. Thus, Cell-4 which allows optimum ionic accessibility (longest plateau), exhibits the highest capacitance retention, as revealed in Fig. 8 (c), and the cell can retain 50 % of its capacitance up to 1 Hz [65].

3.2.3 Specific power and specific energy

Table 7. The values of P_{max} , percentage of power improvement and E_{max} of all the cells.

Ref.	Electrodes	P_{max} (W kg ⁻¹)	Power Improvement (%)	E_{max} (Wh kg ⁻¹)	
Present study	ACM0	155	-	3.5	
	ACM4	215	39	3.1	
	ACM8	194	25	2.5	
	ACM12	179	15	2.0	
	ACM20	162	5	1.4	
[10]	SACG/CNT	0 wt%	158	-	3.82
		5 wt%	160	1	3.54
[36]	SACG/Graphene	0 wt%	104	-	2
		6 wt%	156	50	3
[37]	SACG/Graphene	0 wt%	132	-	0.29
		2 wt%	165	25	1.16
[56]	AC/ Graphene Oxide	0 wt%	-	-	-
		3 wt%	60	-	12
[67]	Porous Carbon/ MWCNT	0 wt%	-	-	-
		1 wt%	200	-	2
[68]	AC/CNT	0 wt%	4400	-	6.04
		5 wt%	7300	66	22.50
[69]	AC/Graphene	0 wt%	50	-	8
		1 wt%	50	0	17

The values of specific power (P) and specific energy (E) calculated using equations (7) and (8) from the GCD curves were used to plot Ragone curve (P versus E) as shown in Fig. 10. All of the cells show a typical specific power-energy relationship commonly found for carbon composite based supercapacitors [66], wherein the specific energy remains almost unchanged at low specific powers and then gradually decreases before exhibiting a relatively larger decrease in the region of high specific powers. The addition of graphite results in a drastic increase in the specific power, and the maximum increase is observed for Cell-4 compared to the Cell-0, which exhibits the lowest specific power. However, the reference cell exhibits the maximum specific energy.

The values of maximum specific power (P_{max}) and maximum specific energy (E_{max}) of the cells determined from the GCD data are shown in Table 7. These values are comparable to the recently reported values of supercapacitors using composite electrodes [10,36,37,56,67–69]. As can be seen in this table that the incremental improvement of P_{max} expressed in percentage achieved in this study are in the range of 5 % to 39 %, which are comparable with that reported in the cited references. These results show that the graphite additive has the potential to improve the power performance of supercapacitors up to a level achieved by using expensive additive such as CNT and graphene. However, a reduction in E_{max} values of the cells is associated with its use.

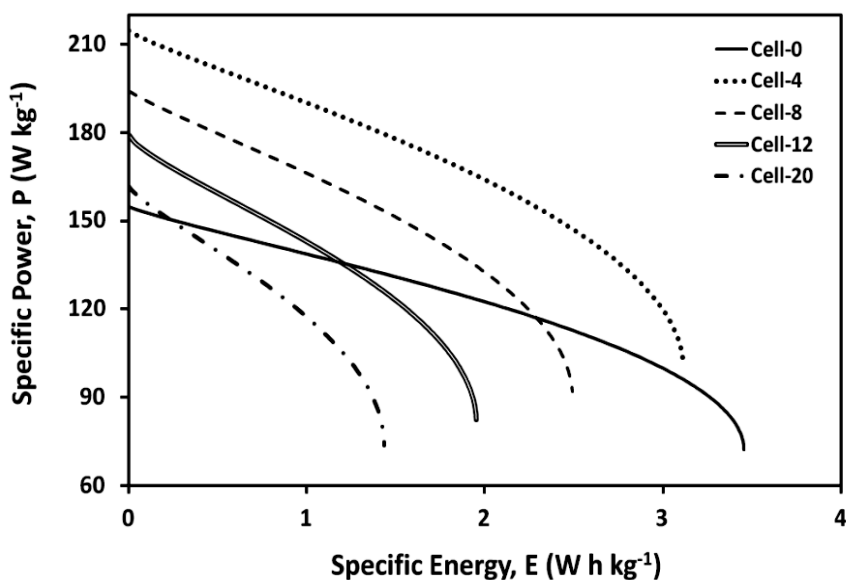


Figure 10. The Ragone curves for all cells.

4. CONCLUSION

Variable amounts (0 to 20 wt%) of graphite powder were mixed with SACGs derived from the fibers of EFB and converted into GMs before activation and carbonization to produce ACM electrodes. The performance of the electrodes was compared with reference electrodes (ACM0). Graphite addition influences the properties of the electrode materials in terms of changes in the structure, microstructure and porosity of the ACM electrode materials. The results based on the EIS, CV, and GCD studies

demonstrate that a graphite content of 4 wt.% in the GMs results in the best performance in terms of *EDR*, *ESR*, τ_o and the specific power of the device. The structural changes leading to the increases in mesoporosity and electrical conductivity of the modified electrodes improve the performance of the cells. A substantial decrease in the *ESR* (~ 70%) and response time, τ_o (~ 87%), leading to a 39% improvement in the specific power were observed with respect to the ACM0 electrode. The τ_o improvement corresponds to an 8-fold increase in the maximum operating frequency, f_{max} (from ~0.13 Hz to ~1 Hz). These results demonstrate that the pre-carbonized biomass fibers can be mixed with cheap graphite to produce more efficient electrodes with improved performances.

ACKNOWLEDGEMENTS

We acknowledge grants from the Ministry of Science, Technology and Innovation (MOSTI) (03-01-02-SF1118), the Ministry of Higher Education (FRGS/1/2016/STG07/UKM/02/2) and the University Kebangsaan Malaysia (DIP-2014-027) and the support from the Centre for Research and Innovation Management (CRIM), UKM. The authors also thank Mr. Saini for help with the laboratory work and for the collaborative work of the Department of Physics and Astrophysics, University of Delhi, India.

References

1. V. Ruiz, C. Blanco, R. Santamaría, J.M. Ramos-Fernández, M. Martínez-Escandell, A. Sepúlveda-Escribano, and F. Rodríguez-Reinoso, *Carbon.*, 47 (2009) 195.
2. X. Lu, M. Yu, G. Wang, Y. Tong, and Y. Li, *Energy Environ. Sci.*, 7 (2014) 2160.
3. X. Hu, N. Murgovski, L. Mardh Johannesson, and B. Egardt, *IEEE Trans. Intell. Transp. Syst.*, 15 (2014) 1193.
4. S.M. Chen, R. Ramachandran, V. Mani, and R. Saraswathi, *Int. J. Electrochem. Sci.*, 9 (2014) 4072.
5. Y. Xue, Y. Chen, M.L. Zhang, and Y. De Yan, *Mater. Lett.*, 62 (2008) 3884.
6. L.G.H. Staaf, P. Lundgren, and P. Enoksson, *Nano Energy.*, 9 (2014) 128.
7. E. Frackowiak, Q. Abbas, and F. Béguin, *J. Energy Chem.*, 22 (2013) 226.
8. N.S.M. Nor, M. Deraman, R. Omar, R. Farma, N.H. Basri, B.N.M. Dolah, N.F. Mamat, B. Yatim, and M.N.M. Daud, *Energy.*, 79 (2015) 183.
9. B.N.M. Dolah, M. Deraman, M.A.R. Othman, R. Farma, E. Taer, Awitdrus, N.H. Basri, I.A. Talib, R. Omar, and N.S.M. Nor, *Mater. Res. Bull.*, 60 (2014) 10.
10. N.H. Basri, M. Deraman, S. Kanwal, I.A. Talib, J.G. Manjunatha, A.A. Aziz, and R. Farma, *Biomass Bioenerg.*, 59 (2013) 370.
11. R. Farma, M. Deraman, A. Awitdrus, I.A. Talib, E. Taer, N.H. Basri, J.G. Manjunatha, M.M. Ishak, B.N.M. Dollah, and S.A. Hashmi, *Bioresour. Technol.*, 132 (2013) 254.
12. M. Deraman, S.K.M. Saad, M.M. Ishak, E. Taer, I. Talib, R. Omar, M.H.H. Jumali, and M. Abdullah, *AIP Conf. Proc.*, 1284 (2010) 179.
13. E. Taer, M. Deraman, I.A. Talib, S.A. Hashmi, and A.A. Umar, *Electrochim. Acta.*, 56 (2011) 10217.
14. M. Suleman, Y. Kumar, and S.A. Hashmi, *J. Solid State Electrochem.*, 19 (2015) 1347.
15. M. Suleman, Y. Kumar, and S.A. Hashmi, *Mater. Chem. Phys.*, 163 (2015) 161.
16. M.M. Ishak, M. Deraman, I.A. Talib, N.H. Basri, Awitdrus, R. Farma, E. Taer, R. Omar, N.S.M. Nor, and B.N.M. Dolah, *AIP Conf. Proc.*, 1656 (2015) 30005.
17. M. Deraman, M.P. Ismail, and M.M. Said, *J. Mater. Sci. Lett.*, 14 (1995) 781.
18. M. Deraman, S. Zakaria, R. Omar, and A.A. Astimar, *Japan J. Appl. Phys.*, 39 (2000) 1236.

19. M. Deraman, R. Omar, and S. Zakaria, *J. Mater. Sci.*, 37 (2002) 3329.
20. E. Taer, Iwantono, S.T. Manik, R. Taslim, D. Dahlan, and M. Deraman, *Adv. Mater. Res.*, 896 (2014) 179.
21. N.H. Basri, M. Deraman, M. Suleman, N.S.M. Nor, B.N.M. Dolah, M.I. Sahri, and S.A. Shamsudin, *Int. J. Electrochem. Sci.*, 11 (2016) 95.
22. Awitdrus, M. Deraman, I.A. Talib, R. Omar, M.H.H. Jumali, E. Taer, and M.M. Saman, *Sains Malays.*, 39 (2010) 83.
23. R. Zulkifli, M. Deraman, R. Daik, M.M. Ishak, N.S.M. Nor, M.R.M. Jasni, S. Soltaninejad, and M. Suleman, *Mater. Sci. Forum.*, 846 (2016) 545.
24. S. Soltaninejad, R. Daik, M. Deraman, Y.C. Chin, N.S.M. Nor, N.E.S. Sazali, E. Hamdan, M.R.M. Jasni, M.M. Ishak, M. Noroozi, and M. Suleman, *Int. J. Electrochem. Sci.*, 10 (2015) 10524.
25. S. Soltaninejad, M. Deraman, R. Daik, N.S.M. Nor, B.N.M. Dolah, N.H. Basri, N.E.S. Sazali, E. Hamdan, and M.R.M. Jasni, *Adv. Mater. Res.*, 1112 (2015) 299.
26. N.H. Basri, M. Deraman, R. Daik, M.T.M. Ayob, M.I. Sahri, N.S.M. Nor, B.N.M. Dolah, and S. Soltaninejad, *Adv. Mater. Res.*, 1112 (2015) 236.
27. R. Farma, M. Deraman, S. Soltaninejad, Awitdrus, E. Taer, M.M. Ishak, N.S.M. Nor, N.H. Basri, B.N.M. Dolah, N.K. Othman, M.A.R. Othman, R. Daik, M. Suleman, and G. Hegde, *Electrochemistry.*, 83 (2015) 1053.
28. N.S.M. Nor, M. Deraman, R. Omar, E. Taer, Awitdrus, R. Farma, N.H. Basri, and B.N.M. Dolah, *AIP Conf. Proc.*, 1586 (2014) 68.
29. M.R.M. Jasni, M. Deraman, E. Hamdan, N.E.S. Sazali, N.S.M. Nor, M.M. Ishak, N.H. Basri, R. Omar, M.A.R. Othman, R. Zulkifli, R. Daik, and M. Suleman, *Mater. Sci. Forum.*, 846 (2016) 551.
30. A.G. Pandolfo, G.J. Wilson, T.D. Huynh, and A.F. Hollenkamp, *Fuel Cells.*, 10 (2010) 856.
31. M. Zhu, C.J. Weber, Y. Yang, M. Konuma, U. Starke, K. Kern, and A.M. Bittner, *Carbon.*, 46 (2008) 1829.
32. D. Weingarth, D. Cericola, F.C.F. Mornaghini, T. Hucke, and R. Kötz, *J. Power Sources.*, 266 (2014) 475.
33. C. Zheng, X. Zhou, H. Cao, G. Wang, and Z. Liu, *J. Power Sources.*, 258 (2014) 290.
34. C. Zheng, W. Qian, and F. Wei, *Mater. Sci. Eng. B Solid-State Mater. Adv. Technol.*, 177 (2012) 1138.
35. N.S.M. Nor, M. Deraman, N.H. Basri, B.N.M. Dollah, R. Omar, S. Soltaninejad, R. Daik, and M.D. Norizam, *Adv. Mater. Res.*, 1112 (2015) 303.
36. M.R.M. Jasni, M. Deraman, M. Suleman, E. Hamdan, N.E.S. Sazali, N.S.M. Nor, S.A. Shamsudin, M.R.M. Jasni, M. Deraman, M. Suleman, E. Hamdan, and N.E.S. Sazal, *AIP Conf. Proc.*, 1710 (2016) 30034.
37. M. Deraman, N.S.M. Nor, N.H. Basri, B.N.M. Dollah, S. Soltaninejad, R. Daik, R. Omar, M.A. Hashim, and M.A.R. Othman, *Adv. Mater. Res.*, 1112 (2015) 231.
38. R. Farma, M. Deraman, Awitdrus, I.A. Talib, R. Omar, J.G. Manjunatha, M.M. Ishak, N.H. Basri, and B.N.M. Dolah, *Int. J. Electrochem. Sci.*, 8 (2013) 257.
39. B.N.M. Dolah, M.A.R. Othman, M. Deraman, N.H. Basri, R. Farma, I.A. Talib, and M.M. Ishak, *J. Phys. Conf. Ser.*, 431 (2013) 12015.
40. M.M. Ishak, M. Deraman, B.N.M. Dolah, M.A.R. Othman, R. Omar, N.H. Basri, N.S.M. Nor, E. Taer, Awitdrus, R. Farma, and A.A. Aziz, *Adv. Mater. Res.*, 1112 (2015) 308.
41. K. Moothi, S.E. Iyuke, M. Meyyappan, and R. Falcon, *Carbon.*, 50 (2012) 2679.
42. S. Arepalli, *J. Nanosci. Nanotechnol.*, 4 (2004) 317.
43. K.S. Kim, Y. Zhao, H. Jang, S.Y. Lee, J.M. Kim, K.S. Kim, J. Ahn, P. Kim, J. Choi, and B.H. Hong, *Nature.*, 457 (2009) 706.
44. T. Xie, W. Lv, W. Wei, Z. Li, B. Li, F. Kang, and Q.H. Yang, *Chem. Commun.*, 49 (2013) 10427.
45. E. Taer, M. Deraman, I.A. Talib, A.A. Umar, M. Oyama, and R.M. Yunus, *Curr. Appl. Phys.*, 10 (2010) 1071.

46. Z. Ryu, J. Zheng, M. Wang, and B. Zhang, *Carbon.*, 37 (1999) 1257.
47. K.S.W. Sing, D.H. Everett, R.A.W. Haul, L. Moscou, R.A. Pierotti, J. Rouquerol, and T. Siemieniewska, *Pure Appl. Chem.*, 57 (1985) 603.
48. H. Chen, F. Wang, S. Tong, S. Guo, and X. Pan, *Appl. Surf. Sci.*, 258 (2012) 6097.
49. H. Li, L. Pan, C. Nie, Y. Liu, and Z. Sun, *J. Mater. Chem.*, 22 (2012) 15556.
50. K. Sheng, Y. Sun, C. Li, W. Yuan, and G. Shi, *Sci. Rep.*, 2 (2012) 1.
51. L. Deng, R.J. Young, I.A. Kinloch, A.M. Abdelkader, S.M. Holmes, D.A. De Haro-Del Rio, and S.J. Eichhorn, *ACS Appl. Mater. Interfaces.*, 5 (2013) 9983.
52. C. Lei, and C. Lekakou, *Surf. Coatings Technol.*, 232 (2013) 326.
53. Y.R. Chen, K.F. Chiu, H.C. Lin, C.L. Chen, C.Y. Hsieh, C.B. Tsai, and B.T.T. Chu, *Solid State Sci.*, 37 (2014) 80.
54. D. Liu, Z. Jia, and D. Wang, *Carbon.*, 100 (2016) 664.
55. Awitdrus, M. Deraman, I.A. Talib, R. Farma, R. Omar, M.M. Ishak, E. Taer, B.N.M. Dolah, N.H. Basri, and N.S.M. Nor, *AIP Conf. Proc.*, 1656 (2015) 30007.
56. L. Jiang, J. Yan, Y. Zhou, L. Hao, R. Xue, L. Jiang, and B. Yi, *J. Solid State Electrochem.*, 17 (2013) 2949.
57. S. Sang, K. Huang, and X. Li, *Eur. Polym. J.*, 42 (2006) 2894.
58. N. Yoshida, T. Ishisaki, A. Watakabe, and M. Yoshitake, *Electrochim. Acta.*, 43 (1998) 3749.
59. C. Portet, G. Yushin, and Y. Gogotsi, *Carbon.*, 45 (2007) 2511.
60. H. Li, J. Luo, X. Zhou, C. Yu, and Y. Xia, *J. Electrochem. Soc.*, 154 (2007) A731.
61. W. Li, J. Liu, and D. Zhao, *Nat. Rev. Mater.*, 1 (2016) 16023.
62. C. Kim, *J. Power Sources.*, 142 (2005) 382.
63. M. Suleman, Y. Kumar, and S.A. Hashmi, *Electrochim. Acta.*, 182 (2015) 995.
64. P. Staiti, and F. Lufrano, *J. Electrochem. Soc.*, 152 (2005) A617.
65. D. Pech, M. Brunet, H. Durou, P. Huang, V. Mochalin, Y. Gogotsi, P.-L. Taberna, and P. Simon, *Nat. Nanotechnol.*, 5 (2010) 651.
66. P.L. Taberna, G. Chevallier, P. Simon, D. Plée, and T. Aubert, *Mater. Res. Bull.*, 41 (2006) 478.
67. D. Schopf, and M. Es-Souni, *Appl. Phys. A.*, 122 (2016) 203.
68. G. Xu, C. Zheng, Q. Zhang, J. Huang, M. Zhao, J. Nie, X. Wang, and F. Wei, *Nano Res.*, 4 (2011) 870.
69. Q. Xie, R. Bao, C. Xie, A. Zheng, S. Wu, Y. Zhang, R. Zhang, and P. Zhao, *J. Power Sources.*, 317 (2016) 133.